

Benchmarking Corruption Robustness of LVLMs: A Discriminative Benchmark and Robustness Alignment Metric

Xiangjie Sui¹, Songyang Li¹, Hanwei Zhu^{2*}, Baoliang Chen³, Yuming Fang⁴, Xin Sun¹
¹City University of Macau ²Nanyang Technological University
³South China Normal University ⁴Jiangxi University of Finance and Economics

Abstract

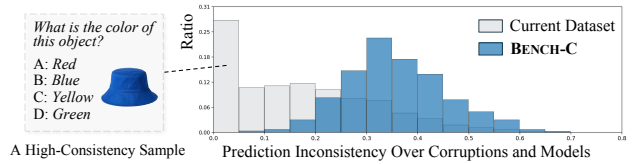
Despite the remarkable reasoning abilities of large vision–language models (LVLMs), their robustness under visual corruptions remains insufficiently studied. Existing evaluation paradigms exhibit two major limitations: 1) the dominance of low-discriminative samples in current datasets masks the real robustness gap between models; and 2) conventional accuracy-based metrics fail to capture the degradation of the underlying prediction structure. To bridge these gaps, we introduce BENCH-C, a comprehensive benchmark emphasizing discriminative samples for assessing corruption robustness, where a selection strategy is proposed to jointly consider the prediction inconsistency under corruption and the semantic diversity. Furthermore, we propose the Robustness Alignment Score (RAS), a unified metric that measures degradation in logit-level prediction structure by considering the shifts in prediction uncertainty and calibration alignment. Comprehensive experiments and analysis reveal several interesting findings: 1) model behaviors exhibit distinguishable patterns under corruptions, such as erroneous confidence and hesitation; 2) despite subtle corruption may lead to a slight accuracy gain, the overall prediction structure still degrades; 3) by decomposing corruption robustness into destructive and corrective components, the distinct failure and recovery patterns across models can be revealed.

1. Introduction

Digital images in the real world are frequently degraded by various types of corruptions, such as compression artifacts, adverse weather conditions, and sensor distortions. While the human visual system exhibits remarkable robustness to such degradations – seamlessly recognizing objects and performing contextual reasoning even under suboptimal conditions [14, 30]. In contrast, modern computer vision systems, particularly large vision–language models (LVLMs),

*Corresponding author (email: hanwei.zhu@ntu.edu.sg)

(a) Dominance of Low-Discriminative Samples



(b) Metric Insensitivity to Prediction Structure Degradation

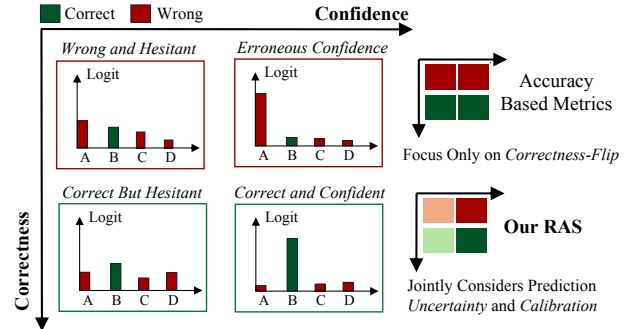


Figure 1. Motivation of this paper. We address two primary limitations – the dominance of low-discriminative samples in evaluation and the metric insensitivity to prediction structure degradation – by introducing a discriminative benchmarking and a structure-aware Robustness Alignment Score (RAS).

exhibit significant fragility when exposed to visual corruptions [19, 37, 40]. This discrepancy underscores a *corruption robustness* gap between human and machine perception, raising questions about how well LVLMs generalize beyond clean data distributions.

Among LVLm evaluation paradigms, multiple-choice question (MCQ) task is widely used due to its intuitive and comparable accuracy metric. For corruption robustness evaluation, previous studies commonly measure the accuracy shift on MCQs constructed with corrupted visual inputs [19, 37, 40]. However, such a paradigm remains two primary limitations, as shown in Fig. 1. First, the evaluation is biased toward a large proportion of low-discriminative

samples that elicit consistent predictions across corruptions and models (see Fig. 1 (a)). Such samples also risk including cases driven mainly by linguistic priors or superficial patterns instead of genuine visual reasoning [3], thereby masking genuine gap in corruption robustness. Second, the accuracy alone obscures the underlying behavioral dynamics of model predictions (see Fig. 1 (b)). For instance, an identical accuracy shift could stem from drastically different behavioral responses *e.g.*, from confidence to hesitation, or vice versa. Thus, accuracy alone offer an incomplete and potentially misleading characterization of model robustness. To address the two limitations, we make two complementary contributions:

- We construct BENCH-C, a *discriminative* benchmark derived from existing datasets that explicitly focuses on the samples which elicit diverse model behaviors under corruption. This benchmark serves as a stress test, emphasizing cases that effectively differentiate robustness across models and reveal vulnerabilities obscured in standard accuracy-oriented evaluations.
- We move beyond accuracy-only assessment by analyzing the *logit distributions* underlying predictions. Building on this, we propose the Robustness Alignment Score (RAS), a unified metric that quantifies fine-grained degradation in prediction uncertainty and calibration alignment, providing a comprehensive measure of corruption robustness.

Overall, BENCH-C and RAS provide a principled framework for understanding corruption robustness of LVLMs. Extensive experiments across 13 state-of-the-art LVLMs reveal significant robustness gaps, with RAS effectively capturing fine-grained model degradation. Moreover, our analysis reveals several key findings, such as 1) distinguish behavior patterns under corruptions, 2) the prediction structure of models consistently degraded under corruptions even with a slight accuracy gain, and 3) diverse failure-recovery dynamics across models. We hope these insights will prompt more reliable and trustworthy deployment of LVLMs in real-world environments.

2. Related Works

In this section, we begin with an overview of LVLMs, followed by two robustness perspectives: adversarial robustness and corruption robustness.

2.1. Large Vision–Language Models

LVLMs have rapidly evolved recently, with research focusing on improving generalization, efficiency, and reasoning capabilities. General-purpose studies [2, 35, 41] advance multimodal integration by enhancing large-context understanding across modalities [35], enabling dynamic-resolution processing [2], and improving long visual-sequence modeling for multi-image or video reasoning [41]. Efficient-oriented studies [1, 9, 27, 28, 39] focus on com-

pact architecture design [1, 27], dynamic tiling vision encoding [39], and high-quality data curation with large-scale multimodal fine-tuning [9, 28]. Reasoning optimization driven studies [5, 8, 17, 22, 25, 33, 36, 38] aim at extending long-context reasoning and structured visual understanding [5, 25, 36], enhancing text-rich and document-level perception and multi-scene description [8, 17, 22, 33], and integrating video-context modeling to generate temporally coherent continuations [38].

2.2. Robustness Evaluation for LVLMs

Model robustness have been studied from several perspectives, *e.g.*, adversarial robustness, corruption robustness, out-of-distribution robustness, etc. Here, we briefly review adversarial and corruption robustness.

2.2.1. Adversarial Robustness

Research on adversarial robustness evaluation typically spans benchmark construction [6, 20, 32], attack taxonomies [7, 23, 26, 44], and defense strategies [12, 13, 21, 29]. Standardized frameworks such as RobustBench [6] and its extensions [20, 32] establish unified protocols and datasets for evaluating adversarial robustness. Researches on attack taxonomy have developed diverse attack paradigms for LVLMs, such as the jailbreak attacks [23, 26] and multimodal attacks [7, 44] that expose the model weaknesses. Another category of research focuses on defense strategies, which explore complementary approaches ranging from traceability [12] and attribution methods [13] to adversarial sample based data augmentation [21] and robust training under structural perturbations [29].

2.2.2. Corruption Robustness

Hendrycks et al. [14] established the foundation of corruption robustness of neural networks by introducing the IMAGENET-C benchmark, demonstrating that high accuracy on clean data does not guarantee robustness to corrupted or distribution-shifted inputs [14, 15]. Ishmam et al. [16] extended this line to the visual question answering domain, and proposed a robustness metric to integrate accuracy drops and prediction errors. Recent efforts have further examined the corruption robustness of LVLMs [19, 37, 40]. Muhammad *et al.* [37] found that text- and image-based reasoning tasks exhibit distinct accuracy degradation patterns to different corruption types. Li *et al.* [19] focus on assessing model robustness under real-world visual corruptions by a text similarity-driven metric [19]. Xing *et al.* [40] identified the visual quality paradox – moderate degradations can unexpectedly improve reasoning accuracy.

3. Problem Definition

Let $\mathcal{Q} = \{(x_i, t_i, y_i)\}_{i=1}^N$ be the set of MCQ instances, where x is the visual input, t is the textual prompt consisting of the question and its K candidate options, and

$y \in \{1, \dots, K\}$ is the ground-truth option index. A LVLMM f maps the pair (x, t) to a vector of option-wise logits: $f : (x, t) \rightarrow z \in \mathbb{R}^K$. The predictive probabilities are obtained via softmax: $p = \text{softmax}(z)$. The predicted answer is the top-1 index: $\hat{y} = \arg \max_{k \in \{1, 2, \dots, K\}} p_k$, where p_k is the probability of k -th option.

For a corruption type $d \in \mathcal{D}$ and a severity level $\ell \in \mathcal{M}$, let $x^{(o)}$ denotes the clean input and $x^{(d, \ell)}$ represents its corrupted counterpart. To quantify the corruption robustness of a model f against visual corruptions, we measure the shift in an evaluation metric Φ on a given sample (x, t, y) :

$$\Delta\Phi^{(d, \ell)} = \Phi\left(f(x^{(d, \ell)}, t), y\right) - \Phi\left(f(x^{(o)}, t), y\right). \quad (1)$$

Aggregating over all corrupted samples yields the overall corruption-induced degradation:

$$\Delta\Phi = \mathbb{E}_{(d, \ell) \sim (\mathcal{D}, \mathcal{M})} \left[\mathbb{E}_{(x, t, y) \sim \mathcal{Q}} [\Delta\Phi^{(d, \ell)}(x, t, y)] \right]. \quad (2)$$

Herein, a critical yet often overlooked factor is the data distribution \mathcal{Q} – a large portion of low-discriminative samples might lead to the aggregated shift $\Delta\Phi$ becoming insensitive to genuine robustness differences. Such an issue can be further amplified when Φ is defined as the accuracy metric: $\Phi = \mathbf{1}\{\hat{y} = y\}$, which captures only the top-1 correctness (*i.e.*, $\max p_k$) while ignoring the richer structural information embedded in the logit distribution p . In this work, we aim at providing a high-discriminative benchmark and moving beyond accuracy to systematically analyze the distributional shifts of p under input degradations, thereby uncovering the latent corruption robustness landscape of LVLMMs.

4. BENCH-C Construction

The construction pipeline of BENCH-C is illustrated in Fig. 2. First, we collect a diverse set of source benchmarks (Sec. 4.1), covering a wide range of tasks and domains. Second, a visual corruption module is introduced to apply diverse corruption types and severity levels levels on visual inputs (Sec. 4.2). Finally, we perform a discriminative sample selection strategy by jointly considering the semantic diversity and discriminative power (Sec. 4.3).

4.1. Source Benchmark Set

BENCH-C is constructed from 6 representative benchmarks that comprehensively cover fine- and coarse-grained perception, understanding, and reasoning:

- SEEDBENCH2+ [18] is a large-scale benchmark emphasizing text-rich visual comprehension and optical character recognition (OCR) related reasoning. It contains approximately 2.3K MCQs involving document images, charts, and visually embedded texts.

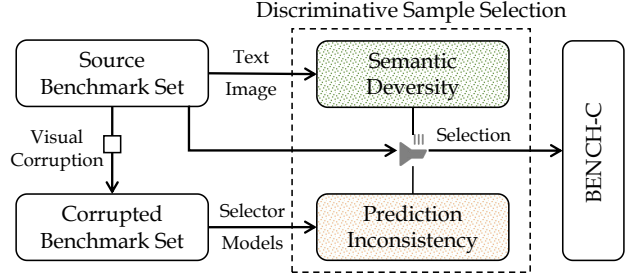


Figure 2. The construction pipeline of BENCH-C. The sample selection strategy integrates both semantic diversity and the prediction inconsistency across corruptions.

- LEGO-PUZZLES [34] targets multi-step spatial reasoning and compositional logic, comprising 1.1K puzzle-style MCQs that require understanding of geometric configurations and object transformations.
- MME-REALWORLD-LITE [43] is a high-resolution collection of about 1.9K real-world visual scenes, spanning outdoor, and traffic environments.
- MMT-BENCH-VA [42] is a multitask benchmark containing more than 3.1K questions covering object recognition, counting, OCR, and commonsense reasoning.
- MMSTARS [4] focus on multi-hop and fine-grained reasoning, which includes 1.5K MCQs that couple textual and visual cues in sequential reasoning chains.
- MMBENCH-DEV-EN-V11 [24] contains roughly 1.2K MCQs across diverse domains such as spatial relations, OCR, temporal reasoning, and visual understanding.

4.2. Visual Corruption

BENCH-C applies 19 corruption types following the IMAGENET-C [14] protocol, grouped into five categories:

- **Photometric:** brightness, contrast, saturation;
 - **Blur:** defocus, gaussian, glass, motion, zoom;
 - **Noise:** gaussian, impulse, shot, speckle;
 - **Weather:** fog, frost, snow, spatter;
 - **Digital:** JPEG compression, pixelation, elastic transform.
- Each corruption type is defined at five severity levels, where higher levels indicate progressively greater degradation.

4.3. Discriminative Sample Selection

To construct a subset that is both discriminative and semantically diverse, we iteratively select samples from the candidate pool \mathcal{A} . At iteration n , the next sample q_n^* is chosen based on:

$$q_n^* = \arg \max_{q \in \mathcal{A} \setminus \mathcal{A}_{n-1}^*} [\alpha_1 \kappa(q) + \alpha_2 \mathbf{D}_s(q, \mathcal{A}_{n-1}^*)], \quad (3)$$

where α_1 and α_2 are trade-off weights, $\kappa(q)$ quantifies the discriminative power of sample q , and \mathbf{D}_s promotes visual-textual diversity by maximizing the semantic distance between q_n^* and \mathcal{A}_{n-1}^* (detailed in Appendix 8.1).

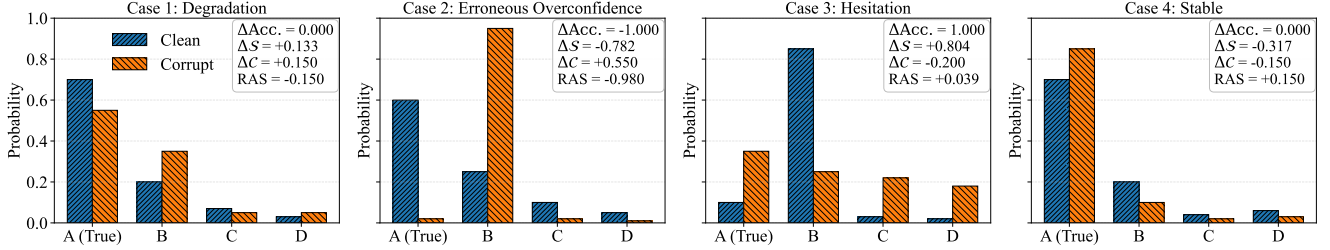


Figure 3. Representative prediction structure shift under corruption. Case 1: *Degradation* (uncertainty $\Delta S \uparrow$, calibration $\Delta C \uparrow$), Case 2: *Erroneous Overconfidence* (uncertainty $\Delta S \downarrow$, calibration $\Delta C \uparrow$), Case 3: *Hesitation* (uncertainty $\Delta S \uparrow$, calibration $\Delta C \downarrow$), and Case 4: *Stable* (uncertainty $\Delta S \downarrow$, calibration $\Delta C \downarrow$).

Discriminative Power $\kappa(q)$. A sample is considered highly discriminative if model predictions vary substantially across corruptions and models. Given a corruption type d , we collect the top-1 predictions of each selector model $f_s \in \mathcal{F}$ across all severity levels: $\hat{y}_{f_s}^{(d)} = \{\hat{y}_{f_s}^{(d,\ell)}\}_{\ell=1}^{\mathcal{M}}$. Let π_{k,f_s} denote the frequency of option k being predicted in $\hat{y}_{f_s}^{(d)}$, the prediction inconsistency is measured by the Gini impurity:

$$\text{Gini}(\hat{y}_{f_s}^{(d)}) = \frac{1 - \sum_{k=1}^K (\pi_{k,f_s})^2}{1 - \frac{1}{K}}. \quad (4)$$

We then average across selector models and corruption types to obtain the overall discriminative power of sample q :

$$\kappa(q) = \frac{1}{|\mathcal{D}||\mathcal{F}|} \sum_{d \in \mathcal{D}} \sum_{f_s \in \mathcal{F}} \text{Gini}(\hat{y}_{f_s}^{(d)}). \quad (5)$$

Higher $\kappa(q)$ indicates stronger prediction inconsistency across both corruptions and models, thus better revealing robustness differences.

4.4. Implementation

Herein, we describe the implementation of BENCH-C construction (more details are presented in Appendix 8.2). Given the source benchmark set, we first balance the number of samples in each task type and by a sampling process, which result in 4K samples (about 200 per task) forming the candidate pool \mathcal{A} . In the discriminative sample selection, we employ three heterogeneous lightweight models as the selector models: MoonDream2 [27], InternVL3-1B [5], and Ovis2-1B [25], and the final $\kappa(q)$ is determined by averaging their results. Then, we filter the samples with $\kappa(q)$ score of zero from \mathcal{A} . The selection process (*i.e.*, Eq. (3)) is iteratively applied $|\mathcal{A}|$ times, with $\alpha_1 = \alpha_2 = 1$. Finally, we preserve the samples whose final scores are above the mean, resulting in $849 \times 19 \times 5 = 80,655$ degraded samples that jointly form BENCH-C. The top-5 question categories include: *Web, Image Retrieval, Map, Chart, and Science & Technology*. Note that the selection is not intentionally biased towards difficult

samples, but rather to adjust the sample distribution toward a more balanced and discriminative regime (see Fig. 1).

5. Robustness Alignment Score

To move beyond accuracy-only evaluation, we first introduce two complementary metrics that jointly capture distinct dimensions of robustness: 1) how predictive uncertainty evolves under input degradation, and 2) how well confidence remains aligned with correctness. We then integrate the two signals into a unified measure, *i.e.*, RAS, to assess the structural robustness of LVM predictions.

Uncertainty Shift (ΔS). Uncertainty shift quantifies how the model confidence changes when inputs are degraded. For a given corruption (d, ℓ) , the normalized entropy of the predictive distribution $p^{(d,\ell)}$ is defined as:

$$\mathcal{S}(p^{(d,\ell)}) = \frac{-\sum_{k=1}^K p_k^{(d,\ell)} \log p_k^{(d,\ell)}}{\log K}. \quad (6)$$

Given the distributions under the clean and the corrupted conditions, the uncertainty shift is then computed as:

$$\Delta S^{(d,\ell)} = \mathcal{S}(p^{(d,\ell)}) - \mathcal{S}(p^{(o)}). \quad (7)$$

$\Delta S \in [-1, 1]$, where $\Delta S > 0$ indicates increased uncertainty, and $\Delta S < 0$ suggests an unexpected increased in confidence despite degraded inputs.

Calibration Shift (ΔC). Calibration shift measures how consistently model confidence corresponds to correctness under degradation. For a given corrupted sample, we define its calibration error as:

$$\mathcal{C}^{(d,\ell)} = |\mathbf{1}\{\hat{y}^{(d,\ell)} = y\} - \max p^{(d,\ell)}|, \quad (8)$$

where $\mathbf{1}\{\hat{y}^{(d,\ell)} = y\}$ indicates correctness, and $\max p^{(d,\ell)}$ indicates the model confidence. The calibration shift is then computed as:

$$\Delta C^{(d,\ell)} = \mathcal{C}^{(d,\ell)} - \mathcal{C}^{(o)}. \quad (9)$$

Table 1. Performance comparison of LVLMs on BENCHMARK-C. \uparrow / \downarrow denotes that higher/lower values are better. The superscripts in $\Delta\text{Acc.}$ and RAS indicate the rank order of the corresponding values (from best to worst of the corruption robustness). Best results are highlighted in **bold** and gray background. Acc.: accuracy; RAS: the robustness alignment score; \mathcal{S} : uncertainty; \mathcal{C} : calibration. For a metric Φ , the superscript (o) indicates the value under clean inputs, and $\Delta\Phi$ indicates the change under visual corruption.

| Model | Year | # of Parameters | Acc. ^(o) \uparrow [0, 1] | $\Delta\text{Acc.}$ \uparrow [-1, 1] | RAS \uparrow [-2, 1] | $\mathcal{S}^{(o)}$ \downarrow [0, 1] | $\Delta\mathcal{S}$ \downarrow [-1, 1] | $\mathcal{C}^{(o)}$ \downarrow [0, 1] | $\Delta\mathcal{C}$ \downarrow [-1, 1] |
|-------------------------------|------|-----------------|--|---|------------------------------|--|---|--|---|
| Emu3-Chat [38] | 2025 | 8B | 0.352 | -0.041 ⁽²⁾ | -0.059 ⁽²⁾ | 0.210 | +0.017 | 0.594 | +0.037 |
| Monkey-Chat [22] | 2024 | 9B | 0.417 | -0.052 ⁽⁴⁾ | -0.076 ⁽⁴⁾ | 0.418 | +0.035 | 0.484 | +0.050 |
| Gemma3 [35] | 2025 | 12B | 0.428 | -0.061 ⁽⁵⁾ | -0.077 ⁽⁵⁾ | 0.079 | +0.011 | 0.567 | +0.056 |
| Falcon2-VLM [28] | 2024 | 11B | 0.441 | -0.040 ⁽¹⁾ | -0.067 ⁽³⁾ | 0.507 | +0.027 | 0.458 | +0.045 |
| Eagle-X5 [33] | 2024 | 7B | 0.451 | -0.069 ⁽⁷⁾ | -0.085 ⁽⁷⁾ | 0.318 | +0.030 | 0.501 | +0.056 |
| mPLUG-Owl3 [41] | 2025 | 7B | 0.465 | -0.049 ⁽³⁾ | -0.059 ⁽¹⁾ | 0.273 | +0.035 | 0.501 | +0.036 |
| Idefics3-Llama3 [17] | 2024 | 8B | 0.561 | -0.094 ⁽¹⁰⁾ | -0.110 ⁽¹²⁾ | 0.078 | +0.029 | 0.431 | +0.088 |
| Molmo [8] | 2024 | 7B | 0.565 | -0.072 ⁽⁸⁾ | -0.088 ⁽⁸⁾ | 0.134 | +0.033 | 0.425 | +0.067 |
| SAIL-VL-1.6 [9] | 2025 | 8B | 0.580 | -0.063 ⁽⁶⁾ | -0.082 ⁽⁶⁾ | 0.219 | +0.012 | 0.390 | +0.060 |
| DeepSeek-VL2-Small [39] | 2024 | 16B | 0.594 | -0.089 ⁽⁹⁾ | -0.093 ⁽⁹⁾ | 0.170 | +0.066 | 0.399 | +0.074 |
| Phi-4-Multimodal-Instruct [1] | 2025 | 6B | 0.604 | -0.098 ⁽¹²⁾ | -0.109 ⁽¹¹⁾ | 0.109 | +0.055 | 0.392 | +0.088 |
| Kimi-VL-A3B-Instruct [36] | 2025 | 16B | 0.630 | -0.096 ⁽¹¹⁾ | -0.105 ⁽¹⁰⁾ | 0.136 | +0.062 | 0.356 | +0.085 |
| Qwen2.5-VL-Instruct [2] | 2025 | 7B | 0.667 | -0.115 ⁽¹³⁾ | -0.129 ⁽¹³⁾ | 0.118 | +0.071 | 0.324 | +0.109 |

$\Delta\mathcal{C} \in [-1, 1]$, with positive values indicating degraded confidence–accuracy alignment (*i.e.*, worse calibration), while negative values suggesting improved reliability.

Robustness Alignment Score (RAS). The RAS provides an integrated measure of robustness by modeling how these two indicators – uncertainty and calibration –interact to reflect the structural stability of predictions. The RAS explicitly rewards desirable behaviors (*e.g.*, reductions in both uncertainty and calibration error) while penalizing misaligned responses. Formally, RAS is defined as:

$$\text{RAS} = -\Delta\mathcal{C} - \underbrace{[\Delta\mathcal{C}]_+ + [-\Delta\mathcal{S}]_+}_{\text{Overconfidence penalty}} - \underbrace{[\Delta\mathcal{S}]_+ + [-\Delta\mathcal{C}]_+}_{\text{Hesitation penalty}}, \quad (10)$$

where $[x]_+ = \max(0, x)$ denotes the positive-part operator. The first term encourages improvements in calibration; the second term penalizes *erroneous overconfidence* cases where the model becomes more certain but less calibrated; the third term penalizes *hesitation* cases where the model becomes less certain despite improved calibration. By construction, $\text{RAS} \in [-2, 1]$, where higher values indicate more structurally robust prediction behavior. We present four representative behavioral regimes under corruption in Fig. 3, which exhibits how RAS and its components disentangle diverse robustness patterns beyond accuracy alone.

6. Experiments and Analysis

Sec. 6.1 first reports the main results on BENCH-C. In Sec. 6.2, we then analyze the interpretability and sensitivity of RAS in characterizing model degradation. Next, Sec. 6.3 provides an in-depth examination of how different visual

corruptions affect model performance. Finally, Sec. 6.4 introduces two complementary notions to provide a nuanced understanding of LVLM behaviors under degradation.

6.1. Main results

We test 13 representative LVLMs on BENCH-C using the open-source toolkit VLMEvalKit [11], covering a diverse range of architectures and training paradigms: Emu3-Chat [38], Monkey-Chat [22], Gemma3 [35], Falcon2-VLM [28], Eagle-X5 [33], mPLUG-Owl3 [41], Idefics3-Llama3 [17], Molmo [8], SAIL-VL-1.6 [9], DeepSeek-VL2-Small [39], Phi-4-Multimodal-Instruct [1], Kimi-VL-A3B-Instruct [36], and Qwen2.5-VL-Instruct [2]. To obtain database-level results for each metric, we adopt a weighted averaging strategy that emphasizes highly discriminative samples through their weights $\kappa(q)$:

$$\Delta\Phi = \frac{\sum_{d \in \mathcal{D}, \ell \in \mathcal{M}} \sum_{q \in \mathcal{Q}} [\kappa(q) \times \Delta\Phi^{(d, \ell)}(q)]}{|\mathcal{D}| |\mathcal{M}|}. \quad (11)$$

Here, $\Delta\Phi^{(d, \ell)}(q)$ denotes the corruption-induced shift of the metric Φ . For the text-similarity metric [19], we prove that such similarity-based metrics collapse to accuracy on MCQ tasks in Appendix 9.1. Table 1 summarizes the aggregated results across all corruption types on BENCH-C, from which we derive two key observations.

First, RAS and $\Delta\text{Acc.}$ are not highly consistent. For instance, Falcon2-VLM [28] outperforms mPLUG-Owl3 [41] in $\Delta\text{Acc.}$, yet the conclusion reverses when evaluated by RAS. This discrepancy suggests that $\Delta\text{Acc.}$ may overestimate robustness by overlooking latent shifts in model re-

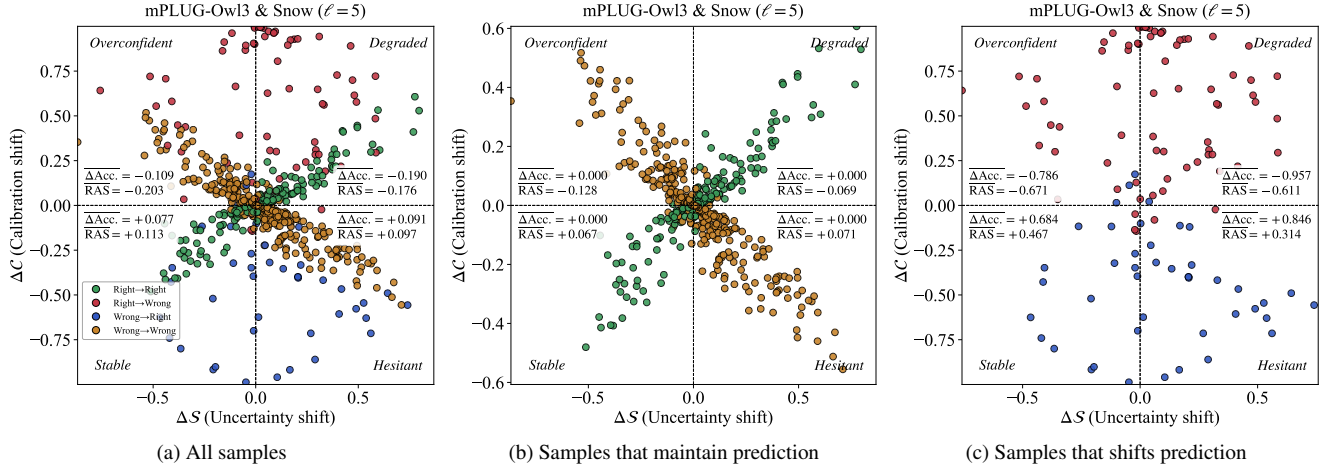


Figure 4. Behavioral analysis of MPLUG-Owl3 under *Snow* corruption ($\ell=5$). Each scatter plot visualizes samples in the $(\Delta S, \Delta C)$ plane, divided into four behavioral types: (*Erroneous*) *Overconfident*, *Degraded*, *Stable*, and *Hesitant*. Panels (b)–(c) isolate samples that maintain or shift predictions. While ΔAcc . measures correctness change, RAS exposes how uncertainty and calibration jointly evolve, revealing structural degradation patterns overlooked by accuracy alone.

liability. RAS, in contrast, captures these internal misalignments by incorporating uncertainty–calibration interactions, thereby revealing confidence drift and calibration errors (further discussed in Sec. 6.2).

Second, models with higher accuracy (on clean inputs) tend to exhibit greater fragility under corruption. For example, Qwen2.5-VL-Instruct [2] achieves the highest accuracy but the lowest RAS, indicating structural instability of predictions under visual degradations. Conversely, Emu3-Chat [38] shows lower accuracy yet smaller RAS degradation. This trend might suggest that high-performance models with better capabilities of capturing fine-grained multimodal cues, are more susceptible to structural perturbations such as *blur*, while low-performance models relying on coarser or less discriminative features might confer partial stability under such perturbations. We further analyze this phenomenon in Sec. 6.3 and Sec. 6.4.

6.2. Analysis of the RAS

How Does the RAS Characters Degradation? To understand how RAS captures the internal structure of model degradation, we project corrupted samples onto the $(\Delta S, \Delta C)$ plane and identify four behavioral regimes: *stable*, *hesitant*, (*erroneous*) *overconfident*, and *degraded*. Each point represents a sample whose position reflects the joint change in uncertainty and calibration under corruption. We further group samples by prediction transitions: *right*→*right* (RR), *wrong*→*wrong* (WW), *right*→*wrong* (RW), and *wrong*→*right* (WR). Fig. 4 (a) visualizes the results for mPLUG-Owl3 [41] under the *snow* corruption at severity level $\ell = 5$. The results reveal that samples with similar accuracy shifts can still exhibit markedly dif-

ferent structural behaviors. Specifically, *overconfident* samples experience the strongest RAS degradation, indicating severe misalignment between confidence and correctness, while *degraded* samples display performance decline consistent with increased uncertainty and calibration error. In contrast, *stable* samples maintain higher RAS values, showing reliable calibration even under uncertainty changes, whereas *hesitant* ones show excessive uncertainty increase without structural failure. These distinct regimes illustrate how RAS disentangles nuanced robustness behaviors, offering a structural perspective on how model reliability deteriorates under corruption.

How Does the RAS Differ From ΔAcc ? While accuracy based metrics only measure correctness flips, RAS characterizes the underlying confidence–accuracy alignment. Fig. 4 (b) and (c) highlight how RAS captures fine-grained structural variations. In Fig. 4 (b) where predictions unflipped, RAS varies considerably (from -0.128 to $+0.071$), indicating that calibration and uncertainty may shift internally even without any correctness change. In Fig. 4 (c), where predictions flip, RAS further distinguishes degradation patterns: samples in the *overconfident* region show the most pronounced internal misalignment. Interestingly, the mean accuracy shifts in the *degraded* quadrant is higher than that in the *overconfident* quadrant, yet the latter exhibits lower RAS values, indicating that RAS is more sensitive to structure collapse than to surface-level accuracy drops. A instance-level comparison in Fig. 5 further shows that RAS captures fine-grained prediction-structure degradation across corruptions. These case studies demonstrate that RAS could complement ΔAcc . by revealing fine-grained prediction-structure degradation, offering improved

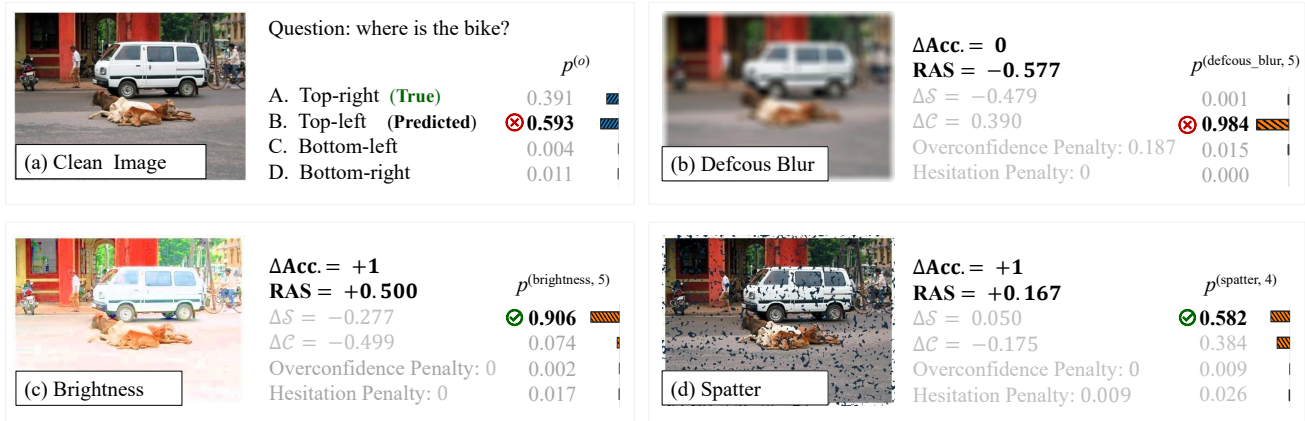


Figure 5. Illustration of robustness analysis of DeepSeek-VL2-Small [39] across corruptions. The model exhibits distinct behavioral patterns. (a) Clean image as reference; (b) Defocus blur causes overconfidence and large RAS drop; (c) Brightness adjustment improves both calibration and confidence, leading to a positive RAS; (d) Spatter leads to correct yet hesitant prediction. The RAS summarizes the shifts in uncertainty (ΔS) and calibration error (ΔC), revealing distinct robustness landscape even when accuracy unchanged.

interpretability of model robustness.

Is the RAS More Sensitive to Visual Quality Than the $\Delta\text{Acc.}$? We further test whether RAS exhibits higher sensitivity to subtle variation of visual quality. For each model and corruption type, we compute the mean absolute z-score of RAS and $\Delta\text{Acc.}$ across adjacent severity levels (i.e., $\ell = m \rightarrow m + 1$), denoted as $\mathbb{E}[|z_{\text{RAS}}|]$ and $\mathbb{E}[|z_{\Delta\text{Acc.}}|]$. A one-sided paired t -test evaluates the hypothesis $H_0 : \mathbb{E}[|z_{\text{RAS}}|] \leq \mathbb{E}[|z_{\Delta\text{Acc.}}|]$, at significance level 0.05. The results reveal that across all tested models and corruption types, $\mathbb{E}[|z_{\text{RAS}}|]$ is significantly higher than $\mathbb{E}[|z_{\Delta\text{Acc.}}|]$ ($p < 0.01$), indicating that RAS responds more sharply to subtle changes in visual quality (see Appendix 9.2 for model-level results), making it a more comprehensive indicator of robustness evaluation.

6.3. Effect of Visual Corruption

How Does Corruption Affects Model Performance? As expected, we found that model performance generally declines as corruption severity increases. However, we observe a counterintuitive phenomenon: several subtle corruptions (i.e., $\ell = 1$) unexpectedly improve accuracy. For instance, Idefics3-Llama3 [17] achieves an accuracy increase from 0.560 to 0.567 under subtle *spatter* distortions. This is consistent with the *visual quality paradox* phenomenon proposed by the recent study [40], which refers to the model performance might be improved even when visual input deviate from human-perceived fidelity. To gain insight into this phenomenon, we analysis all cases where subtle corruptions lead to an unexpected improvement (see Appendix 9.3). We found that such accuracy gains are often *illusory*, arising from prediction instability. This is because the most of these cases correspond to *degraded* or *overconfi-*

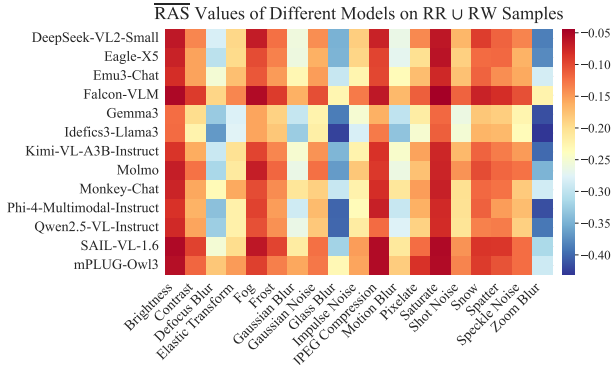
dent patterns, and all cases have negative RAS values. Such results indicate that even though the accuracy increases, the model’s internal prediction structure still deteriorates from a global perspective, suggesting that these improvements are more accidental than indicative of true model robustness.

Which Types of Corruption Most Severely Degrade Model Performance? To address this question, we aggregate RAS scores across models for different visual corruption types and severity levels, highlighting shared vulnerability patterns (see Appendix 9.4 for complete results). Our analysis reveals that the prediction structure of all models consistently degrade as corruption severity increases. Specifically, the structural distortions—such as *blur*-type corruptions and *elastic transformation*—cause the most pronounced degradation. This suggests that corruptions to image structure or semantics significantly impair model behavior. While *noise*-type corruptions (e.g., *impulse noise* and *shot noise*) also yield strong degradation at higher severity, likely due to high-frequency artifacts that disrupt fine-grained features. In contrast, *photometric* (e.g., *brightness*) and *weather* (e.g., *fog*) related corruptions have comparatively mild effects, as they less severely distort object contours and semantics.

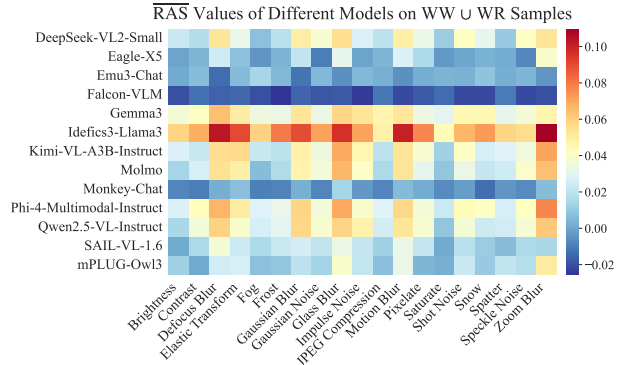
6.4. Analysis of LVL M Corruption Robustness

To further dissect robustness behaviors, we introduce two complementary concepts: *destructive robustness* and *corrective robustness*, which characterize how corruptions affects model prediction structures from distinct perspectives.

Destructive Robustness. Destructive robustness measures a model’s ability to *preserve* structural consistency on samples with correct answers under clean conditions (i.e., $\text{RR} \cup \text{RW}$). Fig. 6 (a) illustrates how visual corruptions af-



(a) Destructive Robustness Matrix



(b) Corrective Robustness Matrix

Figure 6. Destructive and corrective robustness analysis across different corruptions. (a) Destructive robustness analysis, where the RAS values are computed on samples correctly predicted under clean inputs (*i.e.*, $RR \cup RW$). (b) Corrective robustness analysis, where the RAS values are computed on samples mispredicted under clean inputs (*i.e.*, $WW \cup WR$).

fect the destructive robustness of different models, where the cooler hue indicates the lower RAS value and weaker destructive robustness. We can observe that most models exhibit negative RAS values across corruptions, particularly under *blur*-type corruptions, suggesting strong dependence of destructive robustness on structural visual cues. Interestingly, the Falcon-VLM [28] model demonstrates comparatively stronger robustness in this regime, likely due to its high-resolution dynamic encoding mechanism, which enhances fine-grained perception and allows fallback to coarser representations when fine details are lost. Conversely, the models with weaker destructive robustness, *e.g.*, Idefics3-Llama3 [17], might rely on fragile features.

Corrective Robustness. Corrective robustness measures a model’s capacity to (unexpected) improve its prediction structure on previously incorrect samples (*i.e.*, $WW \cup WR$) when inputs are corrupted. As shown in Fig. 6 (b), most models yield near-zero or negative RAS values, revealing that their prediction errors stem from inherent biases rather than being directly caused by corruption. However, certain models exhibit slightly positive RAS, implying that some perturbations can act as implicit regularizers. A notable case is Idefics3-Llama3 [17], whose RAS remains consistently positive across corruptions. However, given the destructive robustness deficits observed earlier, we infer that such improvements may be due to unstable internal representations rather than genuine improvement – perturbations shift the model’s fragile decision boundaries, occasionally producing apparent gains. Therefore, such corrective effects likely arise from instability rather than true robustness.

7. Discussion and Conclusion

In this study, we present BENCH-C, a discriminative benchmark for evaluating the corruption robustness of LVLMs,

along with the RAS, a metric that quantifies degradation from the perspective of internal prediction structure. Extensive experiments and analyses on BENCH-C lead to the following key findings:

- *Patterned Corruption Behaviors.* Model responses to visual corruption follow distinct and structured patterns such as *erroneous confidence* and *hesitation*. These behaviors reveal systematic shifts in confidence–accuracy alignment, even when decision tendencies remain unchanged. Understanding such patterns is essential for diagnosing and improving LVLm robustness.
- *Accuracy–Robustness Decoupling.* Although mild corruptions may occasionally yield slight gains in accuracy, our analysis shows that the underlying prediction structure consistently degrades. This exposes a decoupling between external performance and internal reliability. RAS addresses this gap by capturing latent misalignment between confidence and correctness, offering a more comprehensive measure of corruption robustness.
- *Dual Nature of Corruption Robustness.* The decomposition of robustness reveals complementary failure and recovery patterns across models. The destructive robustness dominates the overall stability of predictions, while corrective robustness reflects a model’s capacity for adaptive recovery. Jointly, they expose a stability–adaptability trade-off underlying robustness, suggesting that an ideal model should preserve structural consistency while allowing meaningful correction under corruption.

While this study offers new insights on corruption robustness, several limitations remain. First, our benchmark primarily involves synthetic corruptions, which do not fully capture real-world degradations [19]. Second, our study focuses on MCQ tasks only, without addressing open-ended reasoning or generative scenarios. Finally, the RAS focuses on the

prediction structure, leaving cross-modal and semantic interactions underexplored. Future work will move toward more naturalistic corruptions and broader task forms for a holistic assessment of LVLM robustness.

References

- [1] Abdelrahman Abouelenin, Atabak Ashfaq, Adam Atkinson, et al. Phi-4-mini technical report: Compact yet powerful multimodal language models via mixture-of-loras. *CoRR*, abs/2503.01743, 2025. 2, 5, 3
- [2] Shuai Bai, Keqin Chen, Xuejing Liu, et al. Qwen2.5-vl technical report. *CoRR*, abs/2502.13923, 2025. 2, 5, 6, 3
- [3] Ellis Brown, Jihan Yang, Shusheng Yang, et al. Benchmark designers should “train on the test set” to expose exploitable non-visual shortcuts. *CoRR*, abs/2511.04655, 2025. 2
- [4] Lin Chen, Jinsong Li, Xiaoyi Dong, et al. Are we on the right way for evaluating large vision–language models? In *Advances in Neural Information Processing Systems*, 2024. 3
- [5] Zhe Chen, Jiannan Wu, Wenhai Wang, et al. Internvl: Scaling up vision foundation models and aligning for generic visual-linguistic tasks. In *IEEE Conference on Computer Vision and Pattern Recognition*, pages 24185–24198, 2024. 2, 4
- [6] Francesco Croce, Maksym Andriushchenko, Vikash Sehwag, et al. RobustBench: a standardized adversarial robustness benchmark. In *Thirty-fifth Conference on Neural Information Processing Systems Datasets and Benchmarks Track*, 2021. 2
- [7] Xuanming Cui, Alejandro Aparcedo, Young Kyun Jang, et al. On the robustness of large multimodal models against image adversarial attacks. In *IEEE Conference on Computer Vision and Pattern Recognition*, pages 24625–24634, 2024. 2
- [8] Matt Deitke, Christopher Clark, Sangho Lee, et al. Molmo and pixmo: Open weights and open data for state-of-the-art vision-language models. In *IEEE Conference on Computer Vision and Pattern Recognition*, pages 91–104, 2025. 2, 5, 3
- [9] Hongyuan Dong, Zijian Kang, Weijie Yin, et al. Scalable vision language model training via high quality data curation. In *Proceedings of the Annual Meeting of the Association for Computational Linguistics*, pages 1595–1612, 2025. 2, 5, 3
- [10] Alexey Dosovitskiy, Lucas Beyer, Alexander Kolesnikov, et al. An image is worth 16x16 words: Transformers for image recognition at scale. *International Conference on Learning Representations*, 2021. 1
- [11] Haodong Duan, Junming Yang, Yuxuan Qiao, et al. VLMEvalKit: An open-source toolkit for evaluating large multi-modality models. In *ACM International Conference on Multimedia*, pages 11198–11201, 2024. 5
- [12] Han Fang, Jiyi Zhang, Yupeng Qiu, et al. Tracing the origin of adversarial attack for forensic investigation and deterrence. In *IEEE International Conference on Computer Vision*, pages 4335–4344, 2023. 2
- [13] Iuri Frosio and Jan Kautz. The best defense is a good offense: Adversarial augmentation against adversarial attacks. In *IEEE conference on computer vision and pattern recognition*, pages 4067–4076, 2023. 2
- [14] Dan Hendrycks and Thomas Dietterich. Benchmarking neural network robustness to common corruptions and perturbations. *International Conference on Learning Representations*, 2019. 1, 2, 3
- [15] Dan Hendrycks, Steven Basart, Norman Mu, et al. The many faces of robustness: A critical analysis of out-of-distribution generalization. In *IEEE international conference on computer vision*, pages 8340–8349, 2021. 2
- [16] Md Farhan Ishmam, Ishmam Tashdeed, Talukder Asir Saadat, et al. Visual robustness benchmark for visual question answering (VQA). In *IEEE Winter Conference on Applications of Computer Vision*, pages 6623–6633, 2025. 2
- [17] Hugo Laurençon, Andrés Marafioti, Victor Sanh, et al. Building and better understanding vision-language models: insights and future directions. *CoRR*, abs/2408.12637, 2024. 2, 5, 7, 8, 3
- [18] Bohao Li, Yuying Ge, Yi Chen, et al. SEED-bench-2-plus: Benchmarking multimodal large language models with text-rich visual comprehension. In *IEEE Conference on Computer Vision and Pattern Recognition*, pages 13299–13306, 2024. 3
- [19] Chunyi Li, Jianbo Zhang, Zicheng Zhang, et al. R-Bench: Are your large multimodal model robust to real-world corruptions? *CoRR*, abs/2410.05474, 2024. 1, 2, 5, 8
- [20] Lin Li, Yifei Wang, Chawin Sitawarin, et al. OODRobustBench: A benchmark and large-scale analysis of adversarial robustness under distribution shift. In *International Conference on Machine Learning*, pages 28830–28869. PMLR, 2024. 2
- [21] Zexin Li, Bangjie Yin, Taiping Yao, et al. Sibling-attack: Rethinking transferable adversarial attacks against face recognition. In *IEEE Conference on Computer Vision and Pattern Recognition*, pages 24626–24637, 2023. 2
- [22] Zhang Li, Biao Yang, Qiang Liu, et al. Monkey: Image resolution and text label are important things for large multimodal models. In *IEEE Conference on Computer Vision and Pattern Recognition*, pages 26763–26773, 2024. 2, 5, 3
- [23] Stephanie Lin, Jacob Hilton, and Owain Evans. TruthfulQA: Measuring how models mimic human falsehoods. In *Proceedings of the 60th Annual Meeting of the Association for Computational Linguistics*, pages 3214–3252, 2022. 2
- [24] Yuan Liu, Haodong Duan, Yuanhan Zhang, et al. MM-bench: Is your multi-modal model an all-around player? In *European Conference on Computer Vision*, pages 216–233. Springer, 2024. 3
- [25] Shiyin Lu, Yang Li, Qing-Guo Chen, et al. Ovis: Structural embedding alignment for multimodal large language model. *CoRR*, abs/2405.20797, 2024. 2, 4
- [26] Weidi Luo, Siyuan Ma, Xiaogeng Liu, et al. Jailbreakv: A benchmark for assessing the robustness of multimodal large language models against jailbreak attacks. In *First Conference on Language Modeling*, 2024. 2
- [27] Inc. M87 Labs. Moondream. In <https://moondream.ai>, 2025. 2, 4

- [28] Quentin Malartic, Nilabhra Roy Chowdhury, Ruxandra Cojocaru, et al. Falcon2-11b technical report. *CoRR*, abs/2407.14885, 2024. [2](#), [5](#), [8](#), [3](#)
- [29] Giorgio Piras, Maura Pintor, Ambra Demontis, et al. Adversarial pruning: A survey and benchmark of pruning methods for adversarial robustness. *Pattern Recognition*, 168:111788, 2025. [2](#)
- [30] Benjamin Recht, Rebecca Roelofs, Ludwig Schmidt, and Vaishaal Shankar. Do CIFAR-10 classifiers generalize to CIFAR-10? *CoRR*, abs/1806.00451, 2018. [1](#)
- [31] Nils Reimers and Iryna Gurevych. Sentence-BERT: Sentence embeddings using siamese bert-networks. In *Proceedings of the 2019 Conference on Empirical Methods in Natural Language Processing*, pages 3980–3990, 2019. [1](#)
- [32] Madeline Chantry Schiappa, Shruti Vyas, Hamid Palangi, et al. Robustness analysis of video-language models against visual and language perturbations. In *Thirty-sixth Conference on Neural Information Processing Systems Datasets and Benchmarks Track*, 2022. [2](#)
- [33] Min Shi, Fuxiao Liu, Shihao Wang, et al. Eagle: Exploring the design space for multimodal llms with mixture of encoders. In *International Conference on Learning Representations*, 2025. [2](#), [5](#), [3](#)
- [34] Kexian Tang, Junyao Gao, Yanhong Zeng, et al. LEGO-Puzzles: How good are mllms at multi-step spatial reasoning? *CoRR*, abs/2503.19990, 2025. [3](#)
- [35] Gemma Team, Aishwarya Kamath, Johan Ferret, et al. Gemma 3 technical report. *CoRR*, abs/2503.19786, 2025. [2](#), [5](#), [3](#)
- [36] Kimi Team, Angang Du, Bohong Yin, et al. Kimi-vl technical report. *CoRR*, abs/2504.07491, 2025. [2](#), [5](#), [3](#)
- [37] Muhammad Usama, Syeda Aishah Asim, Syed Bilal Ali, et al. Analysing the robustness of vision-language-models to common corruptions. *CoRR*, abs/2504.13690, 2025. [1](#), [2](#)
- [38] Xinlong Wang, Xiaosong Zhang, Zhengxiong Luo, et al. Emu3: Next-token prediction is all you need. *CoRR*, abs/2409.18869, 2024. [2](#), [5](#), [6](#), [3](#)
- [39] Zhiyu Wu, Xiaokang Chen, Zizheng Pan, et al. Deepseek-vl2: Mixture-of-experts vision-language models for advanced multimodal understanding. *CoRR*, abs/2412.10302, 2024. [2](#), [5](#), [7](#), [3](#)
- [40] Shuo Xing, Lanqing Guo, Hongyuan Hua, et al. Demystifying the visual quality paradox in multimodal large language models. *CoRR*, abs/2506.15645, 2025. [1](#), [2](#), [7](#)
- [41] Jiabo Ye, Haiyang Xu, Haowei Liu, et al. mPLUG-owl3: Towards long image-sequence understanding in multi-modal large language models. In *International Conference on Learning Representations*, 2025. [2](#), [5](#), [6](#), [3](#)
- [42] Kaining Ying, Fanqing Meng, Jin Wang, et al. MMT-Bench: A comprehensive multimodal benchmark for evaluating large vision-language models towards multitask agi. In *International Conference on Machine Learning*, pages 57116–57198, 2024. [3](#)
- [43] Yi-Fan Zhang, Huanyu Zhang, Haochen Tian, et al. MME-RealWorld: Could your multimodal llm challenge high-resolution real-world scenarios that are difficult for humans? *International Conference on Learning Representations*, 2025. [3](#)
- [44] Yunqing Zhao, Tianyu Pang, Chao Du, et al. On evaluating adversarial robustness of large vision-language models. In *Thirty-seventh Conference on Neural Information Processing Systems*, 2023. [2](#)

Benchmarking Corruption Robustness of LVLMs: A Discriminative Benchmark and Robustness Alignment Metric

Supplementary Material

8. More about BENCH-C

8.1. Discriminative Samples Selection

Diversity formulation. In Eq. 3, the terms D_s encourage diversity of the selected subset in both visual and textual spaces. Herein, we provide a detailed description below. Let $\mathbf{z}_m(q) \in \mathbb{R}^d$ denote the normalized semantic embedding of sample q under modality $m \in \{\text{img}, \text{text}\}$, obtained from a pretrained encoder. Given the already selected set \mathcal{A}_{n-1}^* , we compute the centroid embedding as

$$\mu_m(\mathcal{A}_{n-1}^*) = \frac{1}{|\mathcal{A}_{n-1}^*|} \sum_{q' \in \mathcal{A}_{n-1}^*} \mathbf{z}_m(q'). \quad (12)$$

The diversity score of sample q is defined as the cosine distance between the semantic embedding $\mathbf{z}_m(q)$ and the centroid of the selected set:

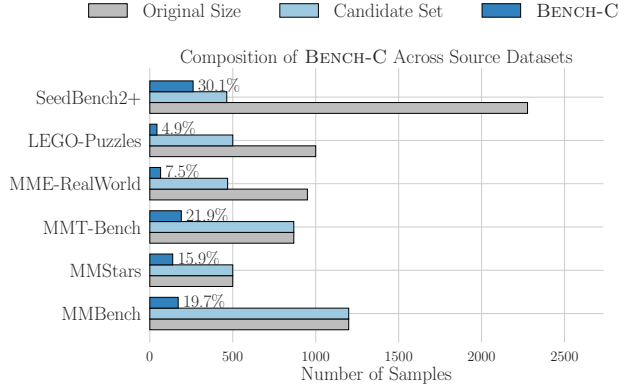
$$D_s(q, \mathcal{A}_{n-1}^*) = 2 - \sum_m \cos(\mathbf{z}_m(q), \mu_m(\mathcal{A}_{n-1}^*)). \quad (13)$$

We adopt ViT-B/32 [10] and Sentence-BERT [31] as the image and text encoders, respectively.

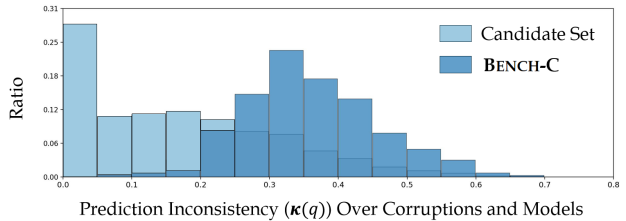
8.2. Composition of BENCH-C

Components of BENCH-C. Fig. 7 (a) summarizes the composition of BENCH-C across six major source datasets. Each horizontal bar shows the number of samples in the original dataset, the candidate pool, and the final curated BENCH-C. Overall, BENCH-C contains 849 samples ($\approx 21.2\%$ of the candidate pool), with SEEDBENCH2+ contributing the largest proportion ($\approx 30.1\%$).

Sample Distribution of BENCH-C. Fig. 7 (b) illustrates the distribution of prediction inconsistency (*i.e.*, discriminative power $\kappa(q)$) across corruptions and models for both the candidate set and the final BENCH-C. The candidate set exhibits a highly skewed distribution concentrated near $\kappa(q) \approx 0$, indicating that a large proportion of samples elicit nearly identical predictions across models and corruption variants, *i.e.*, they are *low-discriminative*. In contrast, the distribution of BENCH-C shifts toward a more balanced and approximately normal shape, centered around higher inconsistency values. This shift reflects the effect of our sample selection strategy, which mitigates the dominance of low-discriminative samples in the candidate set. Fig. 8 presents the number of samples in 27 categories,



(a) BENCH-C consist of six source datasets. Bars indicate the number of samples in the original datasets, candidate pool, and the BENCH-C. The rightmost label shows the percentage of each source in the BENCH-C.



(b) Distribution of prediction inconsistency (*i.e.*, discriminative power $\kappa(q)$) across corruptions and models. BENCH-C provides a more informative and discriminative testbed for evaluating corruption robustness.

Figure 7. The composition of BENCH-C.

which shows that BENCH-C maintains broad tasks. Categories such as *Image Retrieval*, *Web*, *Map*, *Chart* and *Science & Technology* contribute a substantial number of discriminative samples, indicate these tasks are visually demanding or corruption-sensitive. Although some tasks are highly visual reliance, *e.g.*, *Keypoint Detection*, they contribute fewer likely due to they are still non-informative for covering robustness gap. For instance, a sample can be intrinsically difficult yet non-informative for robustness when its corrupted variants elicit uniformly consistent predictions correct or incorrect across models.

Examples with different $\kappa(q)$ To better illustrate the meaning of $\kappa(q)$, Figure 9 presents several representative samples from three $\kappa(q)$ regimes. Samples with low $\kappa(q)$ typically exhibit stable predictions across corruptions and models, either due to their visually trivial nature or weak reliance on nuanced visual information. In contrast, medium $\kappa(q)$ samples involve more visually grounded reasoning,

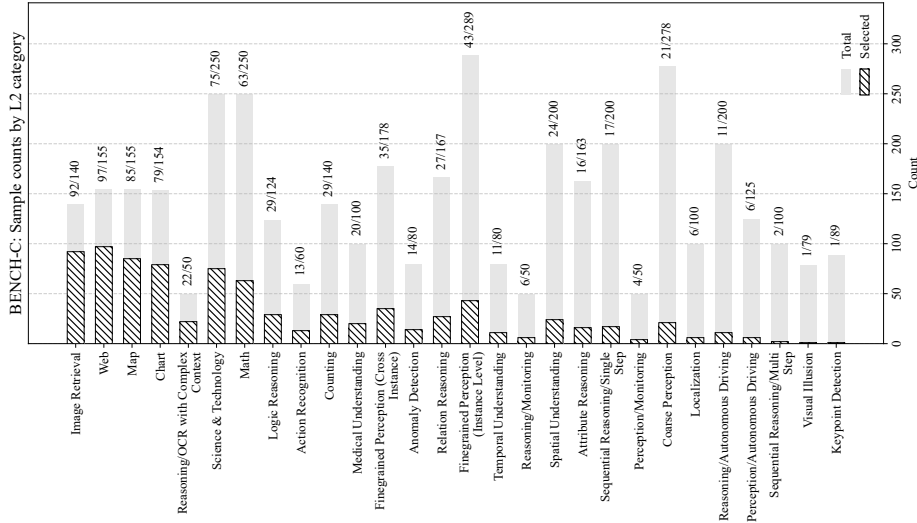


Figure 8. Category-wise sample distribution in BENCH-C. Each bar shows the total number of candidate samples (light gray) and the finally selected high-discriminative samples (hatched).

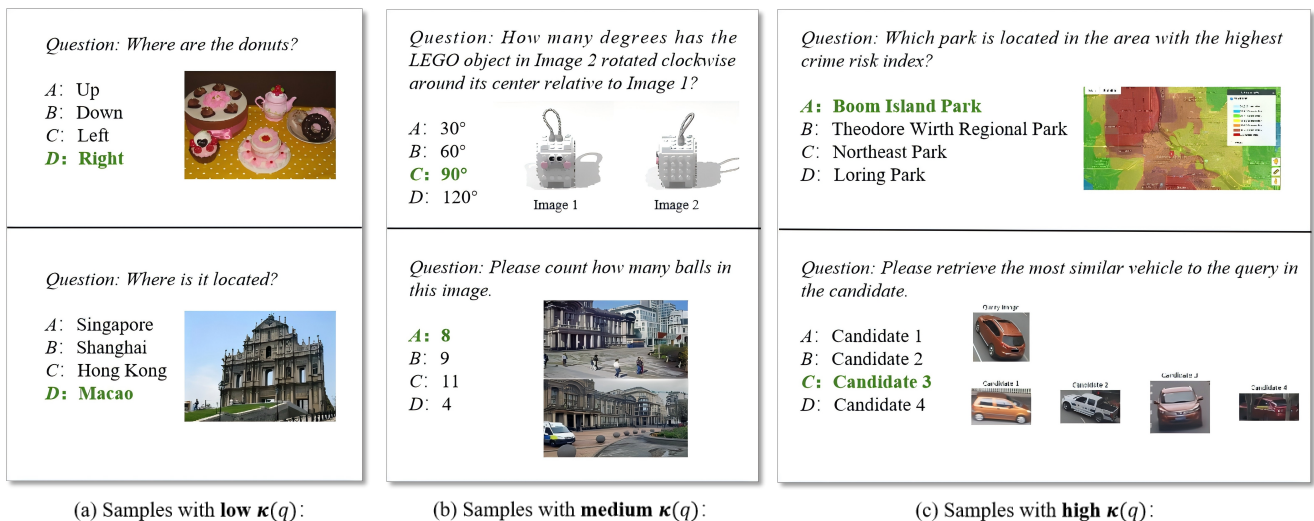


Figure 9. Examples of samples with low, medium, and high discriminative power $\kappa(q)$.

such as rotation, counting, or spatial understanding, which leads to moderate prediction fluctuations. Finally, high $\kappa(q)$ samples require complex, fine-grained, or multi-step visual reasoning, causing models to diverge substantially in their predictions under corruption, thus revealing stronger discriminative power for robustness evaluation.

9. More about Experimental Results

9.1. Similarity-Based Metrics Collapse to Accuracy

Herein, we demonstrate that for MCQ tasks, text similarity based metrics – which measure the average similarity between model generated text and the ground-truth option –

will collapse to accuracy.

Consider an MCQ task with K options, where the model predicts a text response $t_{\hat{y}_i}$ for the i -th sample and the correct option is t_{y_i} . Let $s(\cdot, \cdot) \in [0, 1]$ be a similarity function (e.g., cosine similarity between text embeddings), the similarity-based score across N samples is:

$$\text{Sim} = \frac{1}{N} \sum_{i=1}^N s(t_{\hat{y}_i}, t_{y_i}) \quad (14)$$

$$= \frac{1}{N} \sum_{i=1}^N [\mathbf{1}\{\hat{y}_i = y_i\} \times 1 + \mathbf{1}\{\hat{y}_i \neq y_i\} c_i], \quad (15)$$

where c_i denotes the similarity score when the prediction

is wrong. In MCQ tasks, the prediction space consists of discrete option labels such as “A”, “B”, “C”, “D”, etc, and the similarity is computed on these label tokens. For any two different labels, the similarity score is far below 1 and varies slightly across different incorrect label pairs. Thus, for $\hat{y}_i \neq y_i$, the similarity $s(t_{\hat{y}_i}, t_{y_i})$ can be approximated by a small value, *i.e.*, $c_i \approx c \ll 1$, $\forall i$ with $\hat{y}_i \neq y_i$. Then the similarity score becomes:

$$\text{Sim} \approx \frac{1}{N} \sum_{i=1}^N [\mathbf{1}\{\hat{y}_i = y_i\} + \mathbf{1}\{\hat{y}_i \neq y_i\} c] \quad (16)$$

$$= \frac{1}{N} (N \cdot \text{Acc.} + (N - N \cdot \text{Acc.}) \cdot c) \quad (17)$$

$$= (1 - c) \cdot \text{Acc.} + c. \quad (18)$$

This yields two key conclusions:

- It is a *monotonic linear transformation of accuracy*;
- Model ranking or comparison is therefore *identical*:

$$\text{Acc.}_1 > \text{Acc.}_2 \iff \text{Sim}_1 > \text{Sim}_2.$$

Therefore, the text-similarity metric under MCQ tasks collapses to a monotonic rescaling of accuracy.

9.2. RAS Sensitivity to Visual Quality

Table 2 presents the statistical comparison of the *z-score* normalized RAS and $\Delta\text{Acc.}$ across all corruption types under subtle visual perturbations. For each model, we compute the mean absolute z-scores of RAS and $\Delta\text{Acc.}$, denoted as $\mathbb{E}[|z_{\text{RAS}}|]$ and $\mathbb{E}[|z_{\Delta\text{Acc.}}|]$, respectively. A one-sided paired *t*-test is conducted to test whether RAS exhibits significantly greater sensitivity to visual quality changes than $\Delta\text{Acc.}$, *i.e.*,

$$H_0 : \mathbb{E}[|z_{\text{RAS}}|] \leq \mathbb{E}[|z_{\Delta\text{Acc.}}|].$$

Across all evaluated models, $\mathbb{E}[|z_{\text{RAS}}|]$ consistently exceeds $\mathbb{E}[|z_{\Delta\text{Acc.}}|]$, and the *p*-values are below 0.001 for all cases. The large *t*-statistics (ranging from 35.7 to 70.7) arise from the very small within-group variance after z-score normalization, reflecting a highly consistent superiority of RAS sensitivity rather than an inflated effect size. These results confirm that, even under subtle visual degradations (*e.g.*, $\ell = m \rightarrow m + 1$), RAS is more responsive to variations in perceptual quality than accuracy-based metrics, highlighting its advantage in capturing robustness misalignment behaviors beyond mere accuracy degradation.

9.3. Discussion of Visual Quality Paradox

Table 3 summarizes all cases where subtle corruptions ($\ell = 1$) lead to an unexpected overall increase in accuracy. Although these distortions seem to “improve” model performance in terms of accuracy, a closer inspection of shifts in internal prediction structure reveals such an improvement

Table 2. Statistical comparison of *z-score* normalized RAS and $\Delta\text{Acc.}$ across all corruption types under subtle quality difference (*i.e.*, severity level $\ell = m \rightarrow m + 1$). Results show that RAS exhibits significantly higher sensitivity to visual quality difference.

| Model | $\mathbb{E}[z_{\text{RAS}}]$ | $\mathbb{E}[z_{\Delta\text{Acc.}}]$ | <i>t</i> -statistics | <i>p</i> -value |
|-------------------------------|--------------------------------|---------------------------------------|----------------------|-----------------|
| Eagle-X5 [33] | 0.558 | 0.381 | 51.215 | 2.95e-21 |
| Emu3-Chat [38] | 0.555 | 0.303 | 61.158 | 1.23e-22 |
| Falcon2-VLM [28] | 0.590 | 0.379 | 36.708 | 1.12e-18 |
| Gemma3 [35] | 0.519 | 0.388 | 70.743 | 9.06e-24 |
| Idefics3-Llama3 [17] | 0.555 | 0.444 | 50.858 | 3.35e-21 |
| Kimi-VL-A3B-Instruct [36] | 0.549 | 0.408 | 35.468 | 2.07e-18 |
| Molmo [8] | 0.523 | 0.383 | 49.864 | 4.76e-21 |
| Phi-4-Multimodal-Instruct [1] | 0.550 | 0.414 | 39.183 | 3.51e-19 |
| Qwen2.5-VL-Instruct [2] | 0.576 | 0.442 | 38.953 | 3.90e-19 |
| SAIL-VL-1.6 [9] | 0.564 | 0.391 | 37.117 | 9.21e-19 |
| DeepSeek-VL2-Small [39] | 0.544 | 0.390 | 35.686 | 1.85e-18 |
| mPLUG-Owl3 [41] | 0.535 | 0.344 | 57.424 | 3.81e-22 |
| Monkey-Chat [22] | 0.593 | 0.370 | 57.674 | 3.52e-22 |

might be an illusion. Specifically, among the 28 identified cases, 9 of 28 cases fall into the *overconfident* category, indicating that the accuracy gain might accompanied by over-assertive (erroneous) decision boundaries, which may damage the generalizability. A majority of cases, *i.e.*, 11 of which, exhibit a *degraded* pattern, suggesting a overall degradation trend in prediction structure, even if this is masked by a slight increase in accuracy. There are only 3 and 5 cases corresponding to *hesitant* and *stable* behavior, respectively. Nevertheless, the RAS values indicate the model still degrade overall. This may be because RAS takes into account the shifts in both uncertainty and calibration, making it more effective to capture subtle prediction degradation. We also observe that *spatter* is more likely to lead to an improvement than other corruptions. This might be attributed to the regularization-like nature of the corruption: the random occlusion patterns suppress spurious high-frequency textures and redirect visual attention toward semantically stable regions. Nevertheless, the overall RAS remains negative, which suggests that such improvements may be superficial and only effective for certain questions with strong structural features.

9.4. Analysis of corruption-induced instability.

To investigate which types of visual corruption are more likely to make model predictions unstable, we analyze the RAS distributions across corruption families and severity levels, as shown in Fig. 10. Overall, we observe a clear decreasing trend in RAS as corruption severity increases, indicating that stronger perturbations generally exacerbate degradation and make it more unstable. Among the corruption families, blur type exhibits the most significant degradation, with RAS values sharply dropping. These results indicate that corruptions disrupting spatial structure—such as various forms of blur and *elastic transformation*—

Table 3. Summary of improved Acc. cases under subtle ($\ell = 1$) across models. Cells highlighted in gray represent the *Stable* cases. The RAS values in all cases are negative, revealing the degradation in model performance masked by ΔAcc .

| Model | Distortion | Acc. _{orig} | ΔAcc | Mean ΔS | Mean ΔC | Mean RAS | WR Count | RW Count | Category |
|--------------------|-------------------|----------------------|--------------------|-----------------|-----------------|----------|----------|----------|----------------------|
| Eagle-X5 | Spatter | 0.451 | 0.004 | 0.001 | 0.001 | -0.006 | 14 | 11 | <i>Degraded</i> |
| Emu3-Chat | Snow | 0.352 | 0.009 | 0.002 | 0.005 | -0.020 | 30 | 22 | <i>Degraded</i> |
| Emu3-Chat | Gaussian Noise | 0.352 | 0.007 | -0.001 | 0.002 | -0.014 | 30 | 24 | <i>Overconfident</i> |
| Emu3-Chat | Brightness | 0.352 | 0.005 | -0.005 | 0.009 | -0.016 | 18 | 14 | <i>Overconfident</i> |
| Emu3-Chat | Speckle Noise | 0.352 | 0.002 | -0.002 | 0.013 | -0.025 | 28 | 26 | <i>Overconfident</i> |
| Emu3-Chat | Fog | 0.352 | 0.001 | 0.016 | 0.003 | -0.016 | 35 | 34 | <i>Degraded</i> |
| Falcon2-VLM | Brightness | 0.441 | 0.013 | 0.002 | 0.005 | -0.010 | 40 | 29 | <i>Degraded</i> |
| Falcon2-VLM | Spatter | 0.441 | 0.006 | 0.001 | -0.003 | -0.002 | 29 | 24 | <i>Hesitant</i> |
| Falcon2-VLM | Elastic Transform | 0.441 | 0.004 | 0.001 | 0.022 | -0.043 | 69 | 66 | <i>Degraded</i> |
| Falcon2-VLM | Saturate | 0.441 | 0.002 | -0.003 | 0.012 | -0.019 | 35 | 33 | <i>Overconfident</i> |
| Falcon2-VLM | Motion Blur | 0.441 | 0.001 | 0.011 | 0.026 | -0.042 | 50 | 49 | <i>Degraded</i> |
| Falcon2-VLM | Speckle Noise | 0.441 | 0.001 | 0.005 | 0.014 | -0.026 | 43 | 42 | <i>Degraded</i> |
| Idefics3-Llama3 | Spatter | 0.561 | 0.007 | 0.005 | -0.010 | -0.001 | 25 | 19 | <i>Hesitant</i> |
| Molmo | Contrast | 0.565 | 0.002 | -0.004 | -0.006 | -0.004 | 20 | 18 | <i>Stable</i> |
| SAIL-VL-1.6 | Brightness | 0.580 | 0.006 | -0.016 | -0.001 | -0.007 | 29 | 24 | <i>Stable</i> |
| SAIL-VL-1.6 | Pixelate | 0.580 | 0.006 | -0.008 | 0.004 | -0.019 | 37 | 32 | <i>Overconfident</i> |
| SAIL-VL-1.6 | Contrast | 0.580 | 0.005 | -0.021 | -0.002 | -0.010 | 32 | 28 | <i>Stable</i> |
| SAIL-VL-1.6 | Spatter | 0.580 | 0.005 | -0.014 | -0.003 | -0.002 | 23 | 19 | <i>Stable</i> |
| SAIL-VL-1.6 | Frost | 0.580 | 0.002 | -0.015 | 0.001 | -0.015 | 39 | 37 | <i>Overconfident</i> |
| SAIL-VL-1.6 | Fog | 0.580 | 0.001 | -0.026 | -0.001 | -0.016 | 41 | 40 | <i>Stable</i> |
| SAIL-VL-1.6 | Snow | 0.580 | 0.001 | -0.013 | 0.001 | -0.016 | 37 | 36 | <i>Overconfident</i> |
| DeepSeek-VL2-Small | Brightness | 0.594 | 0.004 | 0.006 | 0.000 | -0.006 | 19 | 16 | <i>Degraded</i> |
| DeepSeek-VL2-Small | Saturate | 0.594 | 0.001 | 0.014 | -0.002 | -0.007 | 22 | 21 | <i>Hesitant</i> |
| DeepSeek-VL2-Small | Snow | 0.594 | 0.001 | 0.023 | 0.002 | -0.011 | 33 | 32 | <i>Degraded</i> |
| mPLUG-Owl3 | Spatter | 0.465 | 0.004 | 0.009 | 0.001 | -0.004 | 12 | 9 | <i>Degraded</i> |
| Monkey-Chat | Gaussian Blur | 0.417 | 0.008 | 0.004 | 0.005 | -0.020 | 48 | 41 | <i>Degraded</i> |
| Monkey-Chat | Elastic Transform | 0.417 | 0.002 | -0.005 | 0.012 | -0.039 | 57 | 55 | <i>Overconfident</i> |
| Monkey-Chat | Speckle Noise | 0.417 | 0.002 | -0.001 | 0.022 | -0.041 | 52 | 50 | <i>Overconfident</i> |

significantly degrade the model’s prediction structure. A exception is *JPEG compression*, which shows a relatively mild impact on RAS, likely due to its preservation of essential semantic features despite introducing compression artifacts. Additionally, noise corruptions (*e.g.*, *impulse noise* and *shot noise*) cause pronounced degradation at severity levels above 3, likely due to their disruption of fine-grained details and the introduction of high-frequency artifacts. In contrast, *brightness* change and several weather-related effects (*i.e.*, *fog*, *frost*, and *snow*) result in relatively minor effects, likely because they have less impact on the contours and semantics of objects.

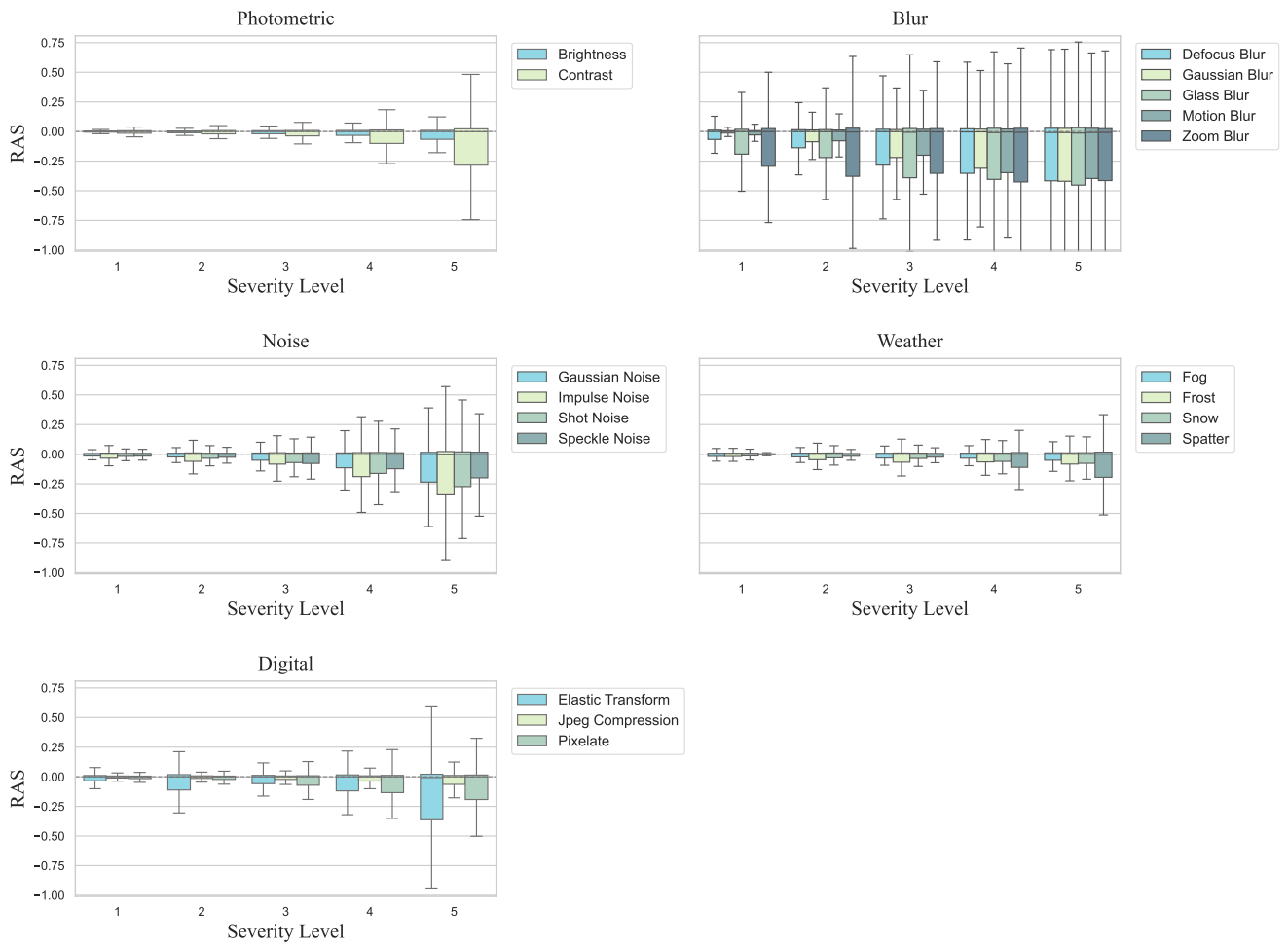


Figure 10. Boxplots of RAS across corruption types and severity levels. Each panel corresponds to one corruption family: Photometric, Blur, Noise, Weather, and Digital.